THE ASTROPHYSICAL JOURNAL, 391:466–482, 1992 June 1

COBE DIFFERENTIAL MICROWAVE RADIOMETERS: CALIBRATION TECHNIQUES

C. L. BENNETT,[1] G. F. SMOOT,[2] M. JANSSEN,[3] S. GULKIS,[3] A. KOGUT,[4] G. HINSHAW,[4] C. BACKUS,[5]
M. G. HAUSER,[1] J. C. MATHER,[1] L. ROKKE,[5] L. TENORIO,[2] R. WEISS,[6] D. T. WILKINSON,[7]
E. L. WRIGHT,[8] G. DE AMICI,[2] N. W. BOGGESS,[1] E. S. CHENG,[1] P. D. JACKSON,[5]
P. KEEGSTRA,[5] T. KELSALL,[1] R. KUMMERER,[5] C. LINEWEAVER,[2]
S. H. MOSELEY,[1] T. L. MURDOCK,[9] J. SANTANA,[5]
R. A. SHAFER,[1] AND R. F. SILVERBERG[1]

Received 1991 October 14; accepted 1991 December 4

ABSTRACT

The *COBE* spacecraft was launched 1989 November 18 UT carrying three scientific instruments into Earth orbit for studies of cosmology. One of these instruments, the Differential Microwave Radiometer (DMR), is designed to measure the large-angular-scale temperature anisotropy of the cosmic microwave background radiation at three frequencies (31.5, 53, and 90 GHz). In this paper we present three methods used to calibrate the DMR. First, the signal difference between beam-filling hot and cold targets observed on the ground provides a primary calibration that is transferred to space by noise sources internal to the instrument. Second, the Moon is used in flight as an external calibration source. Third, the signal arising from the Doppler effect due to the Earth's motion around the barycenter of the solar system is used as an external calibration source. Preliminary analysis of the external source calibration techniques confirms the accuracy of the currently more precise ground-based calibration. Assuming the noise source behavior did not change from the ground-based calibration to flight we derive a 0.1%–0.4% relative and 0.7%–2.5% absolute calibration uncertainty, depending on radiometer channel.

Subject headings: cosmic microwave background — instrumentation: detectors

1. INTRODUCTION

The *Cosmic Background Explorer* (*COBE*),[10] launched into near-polar Earth orbit on 1989 November 18, carries three scientific instruments to investigate fundamental questions in cosmology (Mather 1982; Mather & Kelsall 1980; Gulkis et al. 1990). The Differential Microwave Radiometer (DMR) instrument maps the large-angular-scale ($\theta \gtrsim 3°$) temperature of the cosmic microwave background (CMB) radiation with a 7° beam over the entire sky. The DMR scientific goals, instrument design, and implementation are discussed by Smoot et al. (1990) and early scientific results are reported by Smoot et al. (1991).

In this paper we discuss the techniques available for the calibration of the DMR instrument. The DMR instrument includes radiometers operating at 31.5, 53, and 90 GHz (9.5, 5.7, and 3.3 mm). There are two independent radiometers at each of the three frequencies, henceforth referred to as *channels*, with the radiometers at 31.5 GHz maintained at 300 K and radiometers at 53 GHz and 90 GHz passively cooled to 140 K. This spectral regime was chosen to maximize the intensity ratio of the CMB to the competing galactic foreground emission. The data taken at these three frequencies will allow us to model and remove the local astrophysical radiation. The only celestial emissions detected to date ($>4\ \sigma$) are from the CMB itself (including the dipole anisotropy of the CMB radiation, presumed due to our peculiar motion with respect to the comoving frame of the Hubble expansion), the Moon, and our Galaxy.

We present three independent methods that have been used to calibrate the *COBE* DMRs. The radiometers carry on-board noise sources that were calibrated in the laboratory prior to flight. The definitive analysis of that calibration is presented in this paper. Because that calibration was carried out 15 months before launch, a period of time that included spacecraft vibration testing and thermal cycling, it is desirable to confirm that the calibration did not change by checking the calibration independently in flight. We present two in-flight calibration techniques: (1) based on the microwave signal from the Moon, and (2) based on the microwave signal caused by the Earth-velocity Doppler-shifted CMB. The analysis of these two in-flight techniques is not final since the DMR continues to collect data, and current analysis will be improved, but the analyses to date are important for the choice of calibration for reporting scientific results while the instrument is still taking data. Further improvements, for example in *COBE* attitude solutions, will lead to improved results and analysis will continue.

[1] Laboratory for Astronomy and Solar Physics, NASA/GSFC, Code 685, Greenbelt, MD 20771.
[2] Lawrence Berkeley Laboratory and Space Sciences Laboratory, MS 50-232, UC Berkeley, CA 94720.
[3] Jet Propulsion Laboratory, MS 169-506, 4800 Oak Grove, Pasadena, CA 91109.
[4] University Space Research Association, Code 610.3, NASA/GSFC, Greenbelt, MD 20771.
[5] Hughes STX Corporation, 4400 Forbes Boulevard, Lanham, MD 20706.
[6] MIT, Room 20F-001, Department of Physics, Cambridge, MA 02139.
[7] Princeton University, Department of Physics, Jadwin Hall, Box 708, Princeton, NJ 08544.
[8] UCLA, Astronomy Department, Los Angeles, CA 90024-1562.
[9] General Research Corporation, 5 Cherry Hill Drive, Suite 220, Danvers, MA 01923.
[10] The National Aeronautics and Space Administration/Goddard Space Flight Center (NASA/GSFC) is responsible for the design, development, and operations of the *Cosmic Background Explorer* (*COBE*). Scientific guidance is provided by the *COBE* Science Working Group. GSFC is also responsible for the development of the analysis software and for the production of the mission data sets.

Calibration of the sky temperature scale is required to model the local galactic emission, to quantify the spectrum of the dipole anisotropy, and to specify amplitudes or limits on any other anisotropies. The radiometers are differential, in the sense that they measure power differences between the fields of view of the two horn antennas of each pair, so the term *absolute calibration* refers to the conversion from telemetry counts to temperature of the difference of power received by the two horns. The instrument does not measure the power received by an individual horn. We use the term *relative calibration* to refer to the instrument calibration with respect to a secondary standard, usually to describe changes in the instrument calibration with time. Errors in the absolute calibration can create artifacts in the CMB maps through subtraction of inaccurate galactic models. Time-dependent changes in calibration can create large-scale artifacts in the as-observed DMR sky maps if not properly identified and corrected.

Calibration is performed in terms of an *antenna temperature*, T_A, defined by $T_A \equiv P/k\Delta\nu$, where P is the power received by the radiometer within the filtered intermediate-frequency bandwidth, $\Delta\nu$, referred to the aperture plane of the antenna, and k is Boltzmann's constant. The power the radiometer receives in $\Delta\nu$ from a constant temperature source filling the beam can be written as $P = B_\nu \Delta\nu \lambda^2/2$, where B_ν is the blackbody intensity of the source at frequency ν, λ is the mean wavelength ($= c/\nu$), and the factor of $\frac{1}{2}$ accounts for the single polarization received by an individual radiometer. The error due to the use of a mean wavelength is negligible because of the small fractional bandwidth ($\approx 1\%$). Equating these two expressions for the power gives a relationship between the antenna temperature, T_A, and the thermodynamic temperature, T, of the blackbody covering the antenna aperture, $T_A = T[x/(e^x - 1)]$, where $x \equiv h\nu/kT$ and h is Planck's constant. For a Planckian source, thermodynamic temperature differences can be derived from antenna temperature differences within a bandwidth $\Delta\nu$ by

$$\Delta T = \Delta T_A \frac{[e^x - 1]^2}{x^2 e^x} .$$

Table 1 gives these conversion factors at the three DMR frequencies for a blackbody temperature $T = 2.735$ K. The conversion factor is within 10^{-4} of unity for a 90 GHz radiometer viewing a blackbody target at liquid nitrogen temperature (77 K).

The goal of calibration is to convert a signal strength from raw telemetry *data units* (or *digitization units*, in counts, referred to as *du*'s) to antenna temperature, in mK. For this purpose we define a *gain factor*, $\mathfrak{G}$, with units of du mK^{-1}. Each of the six DMR channels, referred to as 31A, 31B, 53A, 53B, 90A, and 90B, have a distinct gain factor. We determine $\mathfrak{G}$ in flight by observing the output signal deviation produced by a known temperature difference. The three such available signals are from the internal noise sources, the lunar microwave emission, and the Doppler-induced anisotropy in the CMB brightness due to the Earth's motion about the solar system barycenter. Each of these three methods of calibration will be discussed in this paper. For further reading on general properties of microwave radiometers see Evans & McLeish (1977) and Kraus (1966).

TABLE 1

RATIOS OF THERMODYNAMIC TO ANTENNA TEMPERATURES AT THE DMR FREQUENCIES

Frequency (GHz)	Wavelength (mm)	ΔT_{therm} [a] / ΔT_A
31.5	9.52	1.026
53.	5.66	1.074
90.	3.33	1.226

[a] $\Delta T_{therm}/\Delta T_A$ are given for $T_{therm} = 2.735$ K (Mather et al. 1990).

2. GROUND-BASED CALIBRATON TECHNIQUE

In this section we discuss the technique of the calibration of the DMR by use of in-flight noise sources that serve as a transfer standard of the calibration from ground to flight. We present general definitions and describe the method of the ground calibration, describe the calibration and test facility, discuss the analysis of the noise source calibration data taken on the ground, and summarize the in-flight noise source behavior.

2.1. *Definitions and Method*

The basis of the DMR noise source calibration technique is the radiometric comparison of "cold" (~77 K) and "warm" (~300 K) targets. This primary calibration is transferred to solid state noise sources, which inject a small amount of wide-band noise (~2 K) into the front end of the radiometer between the horn antenna and the Dicke switch (Smoot et al. 1990). The noise sources consist of resistor networks for voltage division, and a diode that generates wide-band white noise. There are two independent noise sources at each DMR frequency. Each noise source signal is sent through *both* radiometer channels at its respective frequency. The noise sources provide a positive or negative differential signal depending on which horn the signal is injected into. The noise sources are turned on and off, first for one horn ("up"), then the other ("down"), producing an approximately square-wave reference signal (Fig. 1) that can be compared to the target-derived calibration. The ground calibration determines an antenna tem-

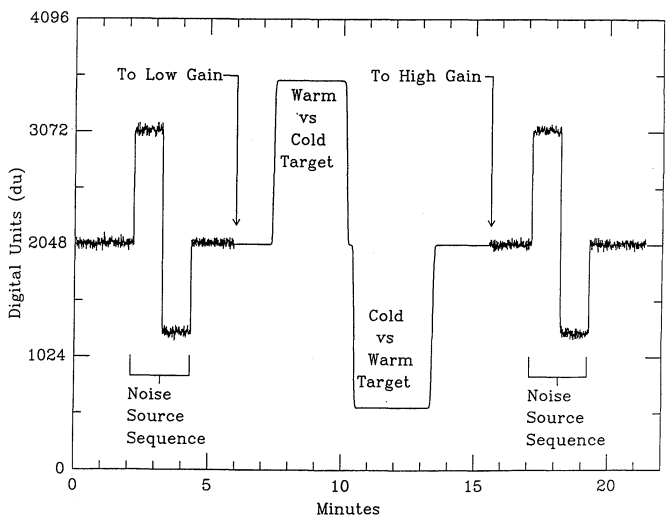

FIG. 1.—Illustrative radiometer output vs. time of a typical ground calibration test procedure. The amplitude of the noise source signals is calibrated by comparison with measurements of microwave targets of known physical temperature.

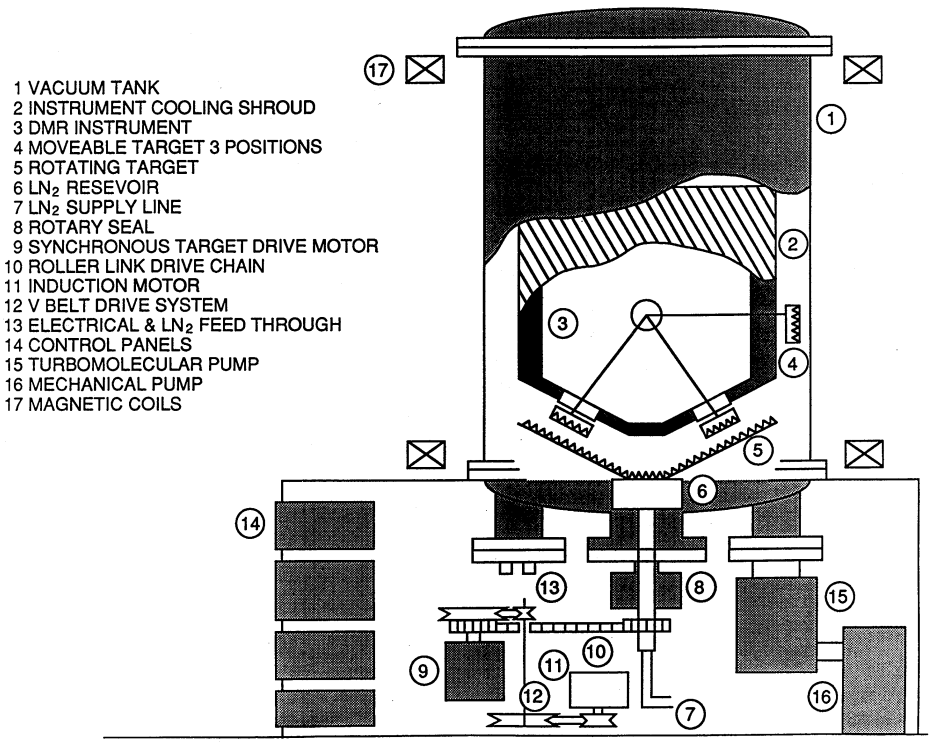

FIG. 2.—Schematic view of the thermal vacuum calibration facility. The radiometer (the large white area) (3) is placed is placed in the large vacuum tank (1) and looks downward toward the large cold spinning target (5), or a movable warm target (4).

perature for the noise source pulses based on known microwave target temperatures.

The noise source amplitudes and gains of the receivers are a weak function of physical device temperatures, complicating the calibration procedure. The DMR had to be calibrated on the ground in as close to an in-flight configuration as possible and over a range of temperatures and conditions. These tests included filling the beam patterns with microwave absorbing targets at known physical temperatures and varying the temperatures of the radiometers to determine the instrument response.

2.2. *Calibration and Test Facility*

The ground calibration of the radiometer systems required a thermally controlled vacuum environment and a system of mechanically and thermally controllable radiometric targets, as shown schematically in Figure 2. The chamber consisted of a 102 × 122 cm stainless steel cylinder with removable end domes. A vacuum was maintained by a turbomolecular pump and its associated mechanical roughing pump. Access to the chamber was provided by six standard 15.24 cm ports located in the bottom end dome.

Both channels at each frequency were tested at the same time in the chamber. The radiometer under test was surrounded by a thermal shroud that could be electrically heated or cooled by liquid nitrogen, which circulated through pipes attached to the shroud walls.

The thermal shroud had openings through which the radiometer antennas viewed microwave targets. These openings were covered with thin Styrofoam panels to allow microwave transmission while minimizing thermal interaction between the targets and horns. A large rotating target consisted of a thermally massive inverted conical aluminum wheel covered with an RF-absorbent material. This target was mounted on a rotating LN_2 reservoir that was filled and maintained through a hollow drive shaft and magnetic fluid rotating vacuum seal. To minimize the effects of temperature variations over the 71.1 cm diameter target, it rotated at a rate synchronous with the data gathering rate of the instrument. The rate was such that a complete rotation of the target occurred for each integration interval of the instrument. Data from each integration period thus represented an average of the target surface temperature over the annulus seen by both antennas. This allows an accurate measurement of the DC offset of the radiometric output with the horns viewing equal temperatures and greatly reduces the effects of any temporal target variations on radiometric characterizations.

A second target consisted of an RF-absorbent material that could be moved into position between either or both of the antennas of a differential radiometer and the rotating target. This second target was equipped with electrical heaters to maintain elevated temperatures and had a thin Styrofoam cover. The second target was used to provide a known temperature difference between the sources in the beams of the differential pair of antennas. It was controlled by a motor driven mechanism that placed it into one of three positions: stowed, where it was out of view of the antennas and isolated from the effects of the cold shroud; or within view of only one antenna; or within view of only the other antenna. The physical temperatures of the RF targets were measured with thermocouples.

External to the chamber, the thermal vacuum calibration facility consisted of vacuum pumps, target rotation motors, liquid nitrogen plumbing, magnetic coils, and system controls.

The rotating target, because of its high inertia, was difficult to drive with available synchronous stepping motors. A belt-connected induction motor was used to start and maintain the target rotation while the synchronous motor maintained lock with the 60 Hz line frequency.

2.3. *Procedure*

The DMR ground calibration consists of two steps: the observation of a known temperature difference, and the proportional transfer of this known difference signal to the difference signal produced by a noise source. The in-flight calibration is based upon this calibrated noise source signal. The absolute calibration results from comparing the differential signal as the radiometer horns alternatively view a warm target covering horn 1 with a cold target covering horn 2, and vice versa. From the signal change, S(du), and the known antenna temperature difference, the radiometer gain factor $\mathfrak{G}$ (du mK^{-1}) (referred to the high gain mode, described below) is determined by:

$$\mathfrak{G} = \frac{R_G(S_{12} - S_{21})}{(T_{12} - T_{21})} = \frac{R_G(S_{12} - S_{21})}{2(T_{\rm warm} - T_{\rm cold})}, \quad (1)$$

where S_{12} and S_{21} are the respective signal levels differentially viewing the warm versus cold and cold versus warm targets, T_{12} and T_{21} are the physical temperature differences between the targets $T_{21} = -T_{12}$ (in mK), and $T_{\rm warm}$ and $T_{\rm cold}$ (in mK) are the antenna temperatures of the two targets. This equation relates the output voltage change to the change in input antenna temperature (or power). The warm and cold microwave targets produced a very large temperature difference (>200 K) compared to the noise source signal (~1 K) and the rms noise of the instrument (~20 mK in 1 s), so the instrument was designed with two gain settings, "high" and "low," with a *gain ratio*, R_G, of about 75 (Smoot et al. 1990). This ratio must be well known so that the fundamental calibration standard consisting of the warm and cold target temperature difference as measured with the "low" gain setting may be accurately transferred to the noise source and ultimately to the measured differential sky brightness temperatures, which are measured with the "high" gain setting.

The "high" versus "low" gain switch is in the lock-in amplifier circuit following the square-law detector diode and the first stage of DC amplification (see Smoot et al. 1990). The ratio of gains between the two switch positions is measured directly in the lock-in amplifier unit. Values of R_G for all channels were obtained prior to the integration of the lock-in amplifiers into the radiometers. In addition, R_G was independently measured through the entire assembled radiometer system during the chamber calibration measurements. These measurements were obtained by comparing the observed digital amplitudes of the noise sources in both low- and high-gain modes, using the averaging of many trials and appropriate "dithering" techniques to compensate for the coarse digitization of the signal in the low gain mode. Both approaches gave consistent results, with our best estimates of the gain ratios, R_G, given in Table 2 with 68% confidence level errors.

The transfer of calibration to the noise sources was accomplished by comparing the signal deviation (in du) produced by the noise sources to the signal deviation produced by the warm and cold targets to determine the antenna temperature of the noise sources. This involved the following steps: (1) turning the noise sources on and off in high-gain mode with both horns viewing a cold target, producing an approximate square-wave output, (2) making a gain measurement in low-gain mode with the warm/cold target permutation described above, and (3) repeating step one by returning to high-gain mode with cold targets. The noise sources were turned on and off immediately before and after the absolute calibration to minimize errors due to drifts in instrument performance. An illustrative radiometer output signal trace of such a sequence is shown in Figure 1.

TABLE 2

GAIN RATIO MEASUREMENTS

Channel	R_G
31A	75.70 ± 0.15
31B	75.37 ± 0.15
53A	75.58 ± 0.10
53B	75.45 ± 0.10
90A	75.56 ± 0.10
90B	75.65 ± 0.10

The antenna temperatures of the noise sources, in mK, are then

$$A_{\rm up} = \frac{S_{\rm up} - S_{\rm base}}{\mathfrak{G}} = \frac{2(T_{\rm warm} - T_{\rm cold})}{R_G}\frac{S_{\rm up} - S_{\rm base}}{S_{12} - S_{21}}, \quad (2a)$$

$$A_{\rm dn} = \frac{S_{\rm dn} - S_{\rm base}}{\mathfrak{G}} = \frac{2(T_{\rm warm} - T_{\rm cold})}{R_G}\frac{S_{\rm dn} - S_{\rm base}}{S_{12} - S_{21}}, \quad (2b)$$

where $S_{\rm up}$ is the signal (in du) with the "up" noise source turned on, $S_{\rm dn}$ with the "down" noise source turned on, and $S_{\rm base}$ is the baseline signal with neither source on. The gain factors and noise source antenna temperatures were calculated using eqs (1) and (2). Computations of both the baseline and noise source levels ignore the first 10 points (5 s) of data to allow a reasonable amount of time to approach thermal stability. The exact method used to calculate the noise source pulse height, S, does not matter provided identical methods are used to calculate ground and in-flight values and that the noise source waveform does not change significantly. The ground and in-flight noise source waveforms are compared in Figure 3, which shows that the average of multiple ground and in-flight noise source turn-ons follow the identical waveforms within the random errors.

Equations (1) and (2) assume the radiometric system is linear with input signal level. To check this assumption, measurements were made to assess the degree of linearity of the radiometers by observing the noise sources, while varying the target temperatures. In all six radiometer channels nonlinearity was determined to be less than 0.5%. We conservatively adopt 0.5% for all channels as the uncertainty in the linearity for the propagation of calibration errors.

Equations (1) and (2) also assume that the target temperatures are accurately known and that they behave as ideal targets. The power reflection loss of the targets was measured, with resulting limits of less than 32 dB at 31.5 GHz and less than 26.5 dB at 90 GHz. These measurements are limited by knowledge of the voltage standing wave ratio (VSWR) of the test horns viewing the targets. We conservatively adopt a total uncertainty for effective target temperature (i.e., for thermometry and emissivity effects) of 1 K at all three frequencies.

The gain factor is measured in flight by turning the noise sources on and off in the standard up/down pattern (see Fig. 1).

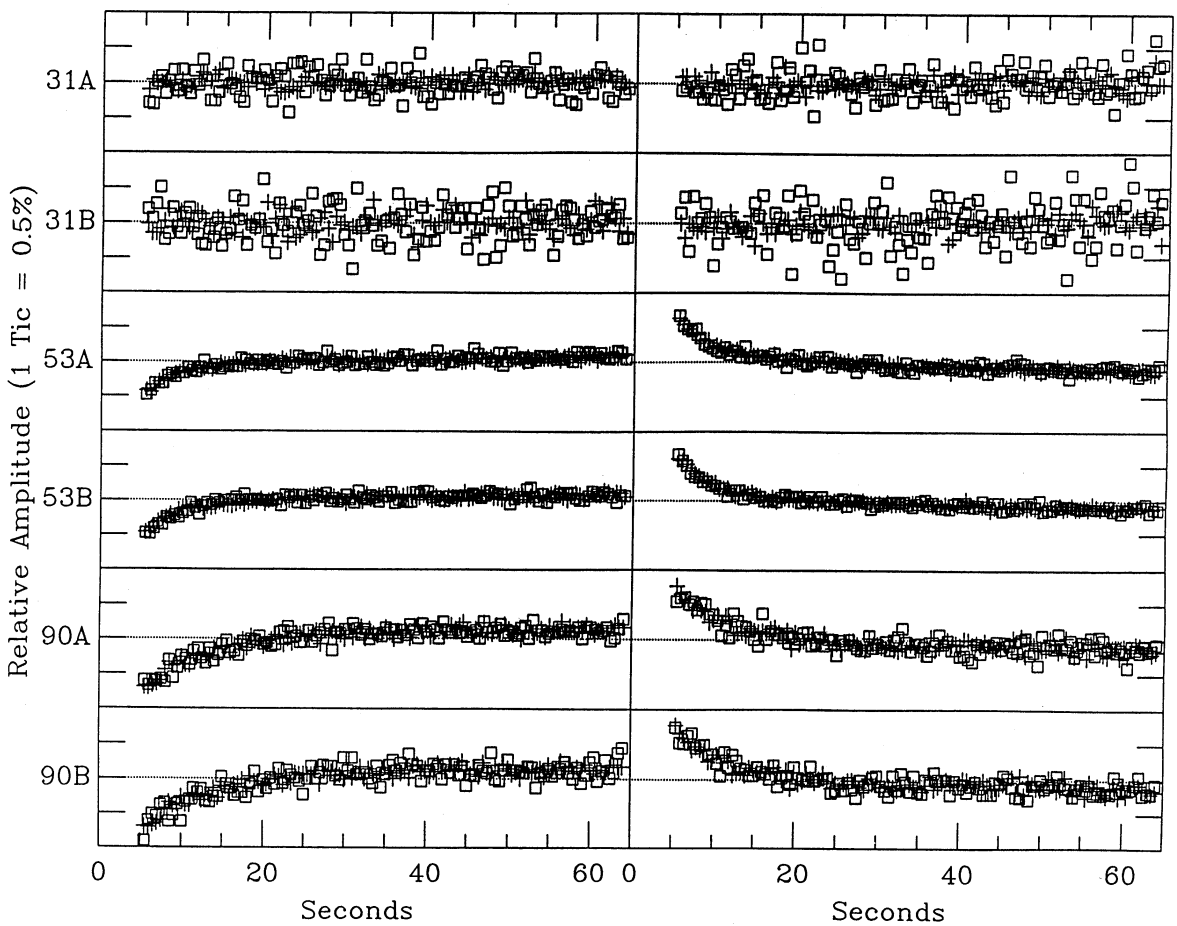

FIG. 3.—These plots show an expanded view of the noise source amplitudes as a function of time while they are turned on (*left:* "up" noise source A; *right:* "down" noise source B). Plots show waveforms for all six channels, and the points represent signal averages of multiple measurements. The boxes are for ground data and + is for flight data. The flight and ground waveforms are seen to be consistent.

The noise sources are activated for 128 s every 2 hr in flight to allow us to account for long-term gain drifts. (See § 2.4 for a discussion of long-term noise source stability.) The flight gain factor, $\mathcal{G}'$, is determined from

$$\mathcal{G}' = \frac{S'_{\rm up} - S'_{\rm dn}}{A'_{\rm up} - A'_{\rm dn}}, \qquad (3)$$

where primed quantities represent in-flight values. The S' are returned by the telemetry, while the A' differ slightly from the A determined on the ground due to thermal effects.

Thermal effects will, in general, change the radiometer calibration both by changing the system gain and the noise source antenna temperature. The thermal corrections are small (<0.5%), but statistically significant. Since we use the noise sources to measure the gain factor in flight, we need to determine the thermal susceptibility of the noise source antenna temperatures. The thermal gain susceptibility cancels in equation (2), leaving only the noise source power output susceptibility. No temperature sensors were placed on the noise sources themselves, so three sensors on other components are used. The three sensors are located on the mixer-preamplifier (MPA) bracket, the local oscillator (LO), and the lock-in amplifier (LIA). We examined the correlation between the noise source output and the temperature determined from these three sensors over a range of temperatures in repeated ground calibration tests. We define a *nominal* temperature, T, as a typical value of the temperature of a component. The choice of nominal temperature has no intrinsic importance; it serves only as a calculational reference point for the thermal susceptibility analysis. Table 3 defines the nominal temperature values used in this paper.

Since the thermal corrections are small, and the temperatures of the MPA, LO, and LIA are highly correlated, we approximate the thermal corrections with a linear dependence on temperature excursion. We use the sensor which produces the highest correlation coefficient. We fit the "up," "down,"

TABLE 3

NOMINAL TEMPERATURES

Component	31A	31B	53A	53B	90A	90B
MPA	295.8	...	139.1	...	139.8	139.8
LO	298.0	298.0	297.6	297.6	...	...
LIA	...	305.9	304.2	302.8	305.4	301.0

NOTE.—MPA = the mixer/preamplifier assembly temperature, LO = the local oscillator assembly temperture, and LIA = the lock-in amplifier assembly temperature. All values are in K. No values are given if the analysis showed no significant thermal susceptibility for that component.

and "peak-to-peak" noise source signals (see Fig. 1), as well as the gain factor, as

$$A'_{up} \equiv A_{up}(T') = A_{up}(T) + \alpha_{up}(\text{comp})[T'(\text{comp}) - T(\text{comp})] , \quad (4a)$$

$$A'_{dn} \equiv A_{dn}(T') = A_{dn}(T) + \alpha_{dn}(\text{comp})[T'(\text{comp}) - T(\text{comp})] , \quad (4b)$$

$$A'_{pp} \equiv A_{pp}(T') = A_{pp}(T) + \alpha_{pp}(\text{comp})[T'(\text{comp}) - T(\text{comp})] , \quad (4c)$$

$$\mathfrak{G}' \equiv \mathfrak{G}(T') = \mathfrak{G}(T) + \beta_g(\text{comp})[T'(\text{comp}) - T(\text{comp})] , \quad (4d)$$

where α_{up}, α_{dn}, and α_{pp}, are the "up," "down," and "peak-to-peak" noise source thermal coefficients (in mK K^{-1}), respectively, β_g is the gain factor thermal coefficient (in du mK^{-1} K^{-1}), primes represent the in-flight values, and "comp" refers to the component (either MPA, LO, or LIA) temperature, whichever produced the best fit. The peak-to-peak noise source amplitudes, A_{pp}, have a distinct calibration advantage in that they do not depend on the evaluation of a baseline level. We fit independently for the peak-to-peak parameters; small inconsistencies that exist between peak-to-peak and a combination of "up" and "down" parameters can be attributed to error in baseline determination.

The fit results for the gain factors and noise source amplitudes at nominal temperature are given in Table 4 and the thermal susceptibilities are given in Table 5. The total uncertainties in Table 4 reflect random errors and systematic errors (uncertainties in target temperature, target emissivity, radiometer nonlinearity limits, analysis uncertainties, and thermal uncertainties).

The gain thermal susceptibility is included only for a consistency check, as discussed in § 2.3.3, and is not used for instrument calibration. If none of the LIA, LO, or MPA fits results in a thermal susceptibility with a correlation coefficient greater than 0.2, the data received no thermal correction. If a solution was found with a correlation coefficient greater than 0.2 then an iteration of the thermal analysis searched for a second most thermally sensitive component in the residual, and removed it if the fit to the second component's thermal susceptibility also showed a correlation coefficient greater than 0.2. Gain thermal coefficients for the 53A, 90A, and 90B channels required a second correction. Since the radiometer noise is insufficient to overcome digitization in the low-gain mode, the statistical uncertainty in the gain coefficient is usually zero.

2.3.1. *Results*

The information in Tables 4 and 5 may be used to derive gain factors and noise source amplitudes off nominal temperature. For example, to calculate the 31A channel flight peak-to-peak noise source amplitude at a LO temperature $T' = 298.5$ K,

$$\begin{aligned} A'_{pp} &= A_{pp} + \alpha_{pp}(T' - T) \\ &= 3638 \text{ mK} + (-25 \text{ mK/K})(298.5 - 298.0 \text{ K}) \\ &= 3626 \text{ mK} . \end{aligned}$$

Least squares fit values are presented for the thermal susceptibilities in all cases where the correlation coefficient is greater than 0.2. The thermal susceptibility coefficients are typically uncertain at about the 50% level, but the uncertainties may be greater or less, depending on the number of test measurements, N, and the value of the correlation coefficient. The maximum range of temperature deviations in-flight for the sensors is less than 0.2 K, and the deviation from the nominal temperatures in Table 3 are also less than 0.2 K. *The thermal susceptibilities affect the final calibration by less than 0.2% so, while their uncertainties are large, their effect on the final result is negligible.*

TABLE 4

NOISE SOURCE AMPLITUDES AND GAIN FACTORS AT NOMINAL TEMPERATURE

Parameter	31A	31B	53A	53B	90A	90B
A_{up} (mK)	2155	1783	2430	2501	1948	1182
rms (mK)	40	33	19	3	7	5
σ_{total} (mK)	54	42	28	17	43	11
σ_{total} (%)	2.5	2.4	1.2	0.7	2.2	0.9
A_{dn} (mk)	−1483	−1362	−2635	−3006	−1557	−1653
rms (mK)	28	30	16	4	4	25
σ_{total} (mK)	38	36	26	22	19	32
σ_{total} (%)	2.6	2.6	1.0	0.7	1.2	1.9
A_{pp} (mK)	3638	3095	5067	5513	3497	2833
rms (mK)	65	58	16	4	7	29
σ_{total} (mK)	91	72	37	39	70	37
σ_{total} (%)	2.5	2.3	0.7	0.7	2.0	1.3
$\mathfrak{G}$ (du/mK)	0.489	0.557	0.520	0.482	0.521	0.611
rms (du/mK)	0.010	0.011	0.006	0.001	0.002	0.006
σ_{total} (du/mK)	0.016	0.014	0.010	0.007	0.004	0.014
σ_{total} (%)	3.3	2.5	1.9	1.5	0.8	2.3

NOTE.—The values are the best estimates of DMR calibration parameters. Mean values, A_{up}, A_{dn}, A_{pp}, and $\mathfrak{G}$, reflect nominal flight operating temperatures. The rms scatter of the distribution and the total uncertainty σ_{total}, which accounts for systematic effects, are given. Peak-to-peak noise source amplitudes are treated independently of the up + down amplitudes, and differ slightly in value because of errors in baseline determination. The down amplitude, A_{dn}, reflects positive antenna temperature in the arm of the radiometer that is subtracted in the differencing and carries a negative sign by our choice of notation.

TABLE 5

THERMAL SUSCEPTIBILITIES OF THE NOISE SOURCE AMPLITUDES AND GAIN FACTORS

Parameter	31A	31B	53A	53B	90A	90B
α_{up} (mK/K)	−14	−16	+11	+9	−38	...
%/K	−0.64	−0.90	+0.45	+0.36	−1.95	...
Component	LO	LIA	MPA	LIA	LIA	...
Corr. coeff.	0.7	0.6	0.3	0.3	0.4	<0.2
α_{dn} (mK/K)	+11	+9	−7	−11	+14	−14
%/K	−0.74	−0.66	+0.27	+0.37	−0.90	+0.85
Component	LO	LO	LO	LO	LIA	MPA
Corr. coeff.	0.7	0.5	0.2	0.5	0.4	0.4
α_{pp} (mK/K)	−25	−27	+16	+20	−64	+11
%/K	−0.69	−0.87	+0.32	+0.36	−1.83	+0.39
Component	LO	LIA	LIA	LIA	LIA	MPA
Corr. coeff.	0.7	0.6	0.6	0.9	0.8	0.3
β_g (du/mK/K)	−0.005	+0.003	+0.007	+0.005	+0.008	+0.010
%/K	−1.	+0.5	+1.	+1.	+2.	+2.
Component	MPA	LIA	LIA	LIA	LIA	LIA
Corr. coeff.	0.7	0.3	0.6	0.5	0.7	0.7
β_g (du/mK/K)	...	...	−0.01	...	−0.003	...
%/K	...	...	−2.	...	−0.6	...
Component	...	...	MPA	...	MPA	...
Corr. coeff.	...	...	0.3	...	0.4	...
N	19	17	35	6	7	7

NOTE.—Fit results to N ground tests for each radiometer channel are shown. Ellipsis dots indicate no significant thermal susceptibility was found. The gain factors for channels 53A and 90A have two thermal corrections; however, these are used only for consistency checks, not for the calibration of the DMR (see § 2.3.3). Although fit values are presented for the thermal susceptibilities in all cases where the correlation coefficient is greater than 0.2, the uncertainties in these susceptibilities may be substantial, especially in cases of a small number of test measurements, N, and/or small correlation coefficients. In no case should the thermal susceptibilities be attributed directly to any specific component. The thermal susceptibilities affect the final calibration by less than 0.2% so, while their uncertainties are large, their effect on the final result is negligible.

The values for S', $A(T)$, α, and T' are known so the in-flight calibration is derived from equations (3) and (4) as

$$\mathfrak{G}' = \frac{S'_{up} - S'_{dn}}{A_{up} - A_{dn} + \alpha_{up}(T' - T) - \alpha_{dn}(T' - T)}, \quad (5)$$

or

$$\mathfrak{G}' = \frac{S'_{pp}}{A_{pp} + \alpha_{pp}(T' - T)}. \quad (6)$$

We prefer the use of equation (6) since it eliminates errors that may arise in baseline determination.

2.3.2. *Consistency Checks*

A consistency check on the gain factor calculation comes from comparison of the result of equation (6) with the value for $\mathfrak{G}$ obtained from equation (4d) with $\mathfrak{G}$ and β_g from Tables 4 and 5. Since the noise source thermal dependences are both smaller and better understood than the gain thermal dependence, equation (6) is the preferred method to calculate the flight gain factor. It remains instructive to compare the two methods as a cross-check. This check was performed in the laboratory, and it was found that the direct calculation of the gain factor accounting for its thermal dependence agreed to within 5% with the much more accurate values determined from the noise sources for all six radiometer channels.

Direct measurements of the noise source amplitude, S', as a function of temperature provide a second consistency check. The output signal change caused by a noise source signal is proportional to the product of the susceptibilities of the noise sources and the gain of the RF chain. In general, the noise sources and RF chain will both deviate from nominal temperature simultaneously. Ground tests of the entire spacecraft system in a solar environmental simulator provide a measurement of the thermal susceptibility of the noise source signals, S'. In these tests, the component temperatures were slowly varied off-nominal temperature while turning on the noise sources every 15 minutes. The observed signal variation (in du) is composed of a gain variation *and* a noise source emitted power variation. Comparison of the measured thermal susceptibilities in S' from the solar environmental simulator tests with predicted susceptibilities based on the thermal vacuum calibration facility tests provides a consistency check on the estimates of the thermal susceptibilities of the DMR. The values agree to better than 50% (the approximate error in the thermal coefficients), indicating that the small thermal susceptibilities of the gain factor and noise sources have been determined to the ~50% level.

2.4. *In-Flight Stability of the Noise Source Signals*

We have applied the ground-based noise source calibration, as described above, to the in-flight operation of the instrument for the first year of flight. In this section we address the stability of the noise source signals in the first flight year. This *relative*

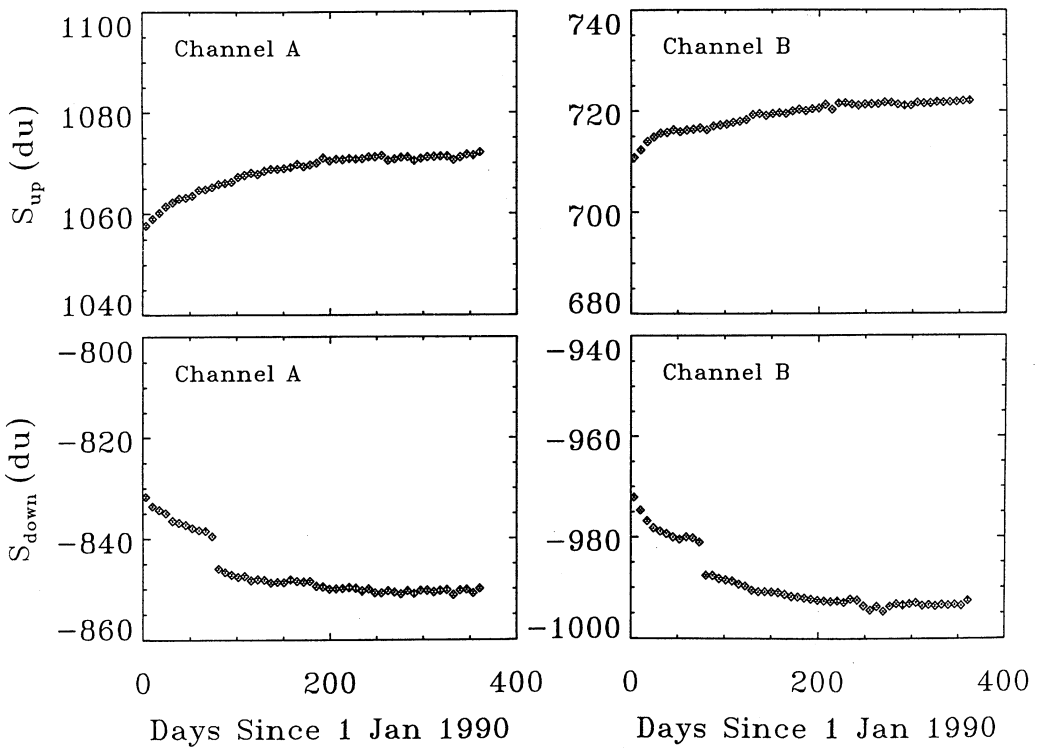

FIG. 4*a*

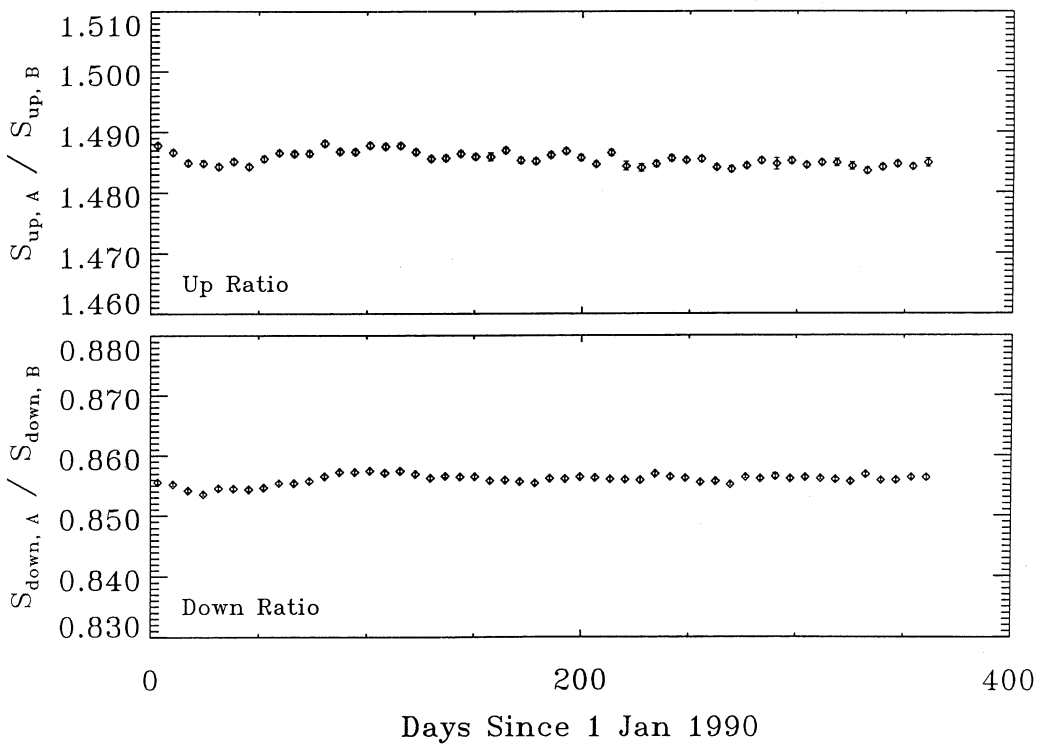

FIG. 4*b*

FIG. 4.—Plots of the 90 GHz noise source ratio values to determine the occurrence of gain constant or noise source amplitude changes with time. The 0.7% change in the 90 GHz "down" noise source is not accompanied by a change in the instrument gain.

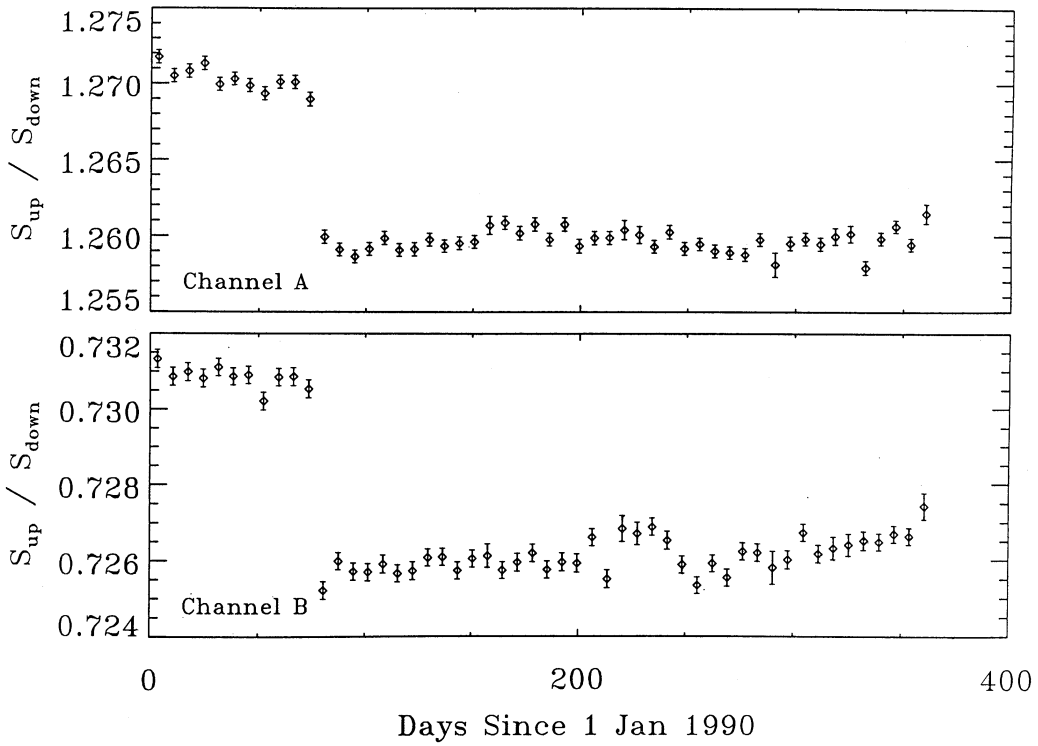

FIG. 4c

calibration check is done by examining the following noise source signal ratios as a function of time at each frequency:

$$\frac{\text{"up" amplitude as seen in channel A}}{\text{"up" amplitude as seen in channel B}},$$

$$\frac{\text{"down" amplitude as seen in channel A}}{\text{"down" amplitude as seen in channel B}},$$

$$\frac{\text{"up" amplitude as seen in channel A}}{\text{"down" amplitude as seen in channel A}},$$

$$\frac{\text{"up" amplitude as seen in channel B}}{\text{"down" amplitude as seen in channel B}}.$$

Independent of the absolute calibration of the noise sources, these ratios will reveal a change in either calibration or noise source amplitude as a function of time and assist in distinguishing between the two. This can be seen in Figure 4, which shows the only time a large sudden change was seen in flight. In this case the "down" noise source in the 90 GHz radiometer increased by 0.7% in amplitude on the 77th day of 1990 at 1100 GMT.

We have examined these ratios for all of the first year data. The noise source signals through the first year of flight were stable to less than 0.4%, relative to one another, except in the single case noted above. This limit assumes that the independent "up" and "down" noise source amplitudes do not vary in amplitude as a function of time in tandem. The lunar and Earth-velocity calibration techniques, described in §§ 3 and 4, can be used to check this assumption, typically to within a couple of percent.

3. IN-FLIGHT CALIBRATION FROM OBSERVATIONS OF THE MOON

3.1. *Introduction*

The Moon is a strong microwave source with known position in the sky and, within the limits of a model for the lunar microwave emission, predictable radiative flux. It is therefore potentially useful as an independent calibrator of parameters of the DMR experiment that are related to the instrumental gain, beam pattern, and pointing. Gain parameters that may be investigated by Moon observations include the absolute gain factors of each channel, the relative calibration across channels, and the long-term time dependence of both.

The DMR instrument observes an antenna temperature due to the Moon within an integration time, τ, as

$$T_{A,\text{Moon}} = \frac{1}{\tau}\int_t^{t+\tau} dt \int d\Omega\, T_{\text{Moon}}\, P[\theta(t), \phi(t)] \Big/ \int d\Omega\, P(\theta, \phi)\,,$$

where T_{Moon} is the radiometric temperature of the Moon, which depends on frequency, polarization, the distance of the Moon from *COBE*, the lunar phase, and the position (θ, ϕ) of the Moon with respect to the DMR beam center. $P(\theta, \phi)$ is the antenna gain pattern normalized such that $P(0, 0) = 1$.

The region of the sky observed by a DMR antenna in a given orbit may be roughly approximated as a swath of 60° width centered on a great circle that passes near the ecliptic poles. This swath slowly precesses with time to remain perpendicular to the Earth-Sun line. The Moon passes through this swath twice in each of its orbits around the Earth, or once approximately every 14 days on alternating sides of the Earth, and is observable for a period of ~6 days during each passage. The peak antenna temperature produced by the Moon in the

beam of a DMR antenna is nearly 1 K, comparable to that of a DMR noise source.

3.2. *The Lunar Model*

The angular diameter of the Moon (~0°.5) is much smaller than a DMR beamwidth (~7° full width at half-power), and the parameters of a lunar emission model required for our purposes are the disk-averaged brightness temperatures at the DMR frequencies and polarizations, the Moon's solid angle as seen from the *COBE* spacecraft, and the centroid positions of the emission. These quantities need only be determined over the limited range of lunar phase angle, φ, in which the Moon is visible in the DMR antennas. Due to *COBE*'s orbital geometry this range is limited to approximately $-90° \pm 30°$ and $+90° \pm 30°$.

The thermal microwave emission from a surface element on the Moon depends upon its roughness and physical properties with depth (complex dielectric constant, density, heat capacity, and thermal conductivity), the angle of emission, and its thermal history. The microwave brightness temperature can be predicted as a function of frequency and lunar phase to the extent that these quantities can be specified from existing data. The Moon's potential as a microwave calibration source has evolved considerably over the past 25 yr from remote observations, in situ experiments, and returned samples. The agreement between Earth-based measurements and theoretical models based on *Apollo* ground-truth data supports the representativeness of local measurements on a global scale (Keihm & Langseth 1975). In addition, comparisons of numerically convolved high-resolution brightness temperatures (Keihm & Gary 1979) support a model of uniform regolith properties on a scale of ~250 km. Centimeter-wavelength contrasts in mare/highland brightness temperatures and in other regional anomalies are less than 4 K; in addition, comparison of measured center-to-limb brightness temperature variations with theoretical predictions indicate that roughness effects are not large. Thus, a uniform "average" global model for unresolved lunar measurements was formulated by Keihm (1983), using thermal and radiative transfer elements as described by Keihm & Langseth (1975). The model predicts the distribution of the brightness temperature across the lunar disk as a function of lunar phase angle, frequency, and linear polarization (parallel or perpendicular to the lunar equator), from which it determines disk-averaged brightness temperatures in two linear polarizations at each frequency as well as the position of the brightness centroid as a position offset from the disk center. Figure 5 shows a plot of disk temperature versus phase angle and polarization at the DMR frequencies computed with this model. Note that the DMR measures the Moon on the steepest portions of the curves.

If the Earth-Moon system were perfectly circular in its orbit around the Sun and the lunar equatorial plane were parallel to the ecliptic, the model would be fully specified by the lunar phase, observing frequency, and polarization. The eccentricity of the Earth's orbit leads to a predicted small (~1 K) annual variation in the daily average surface temperature. This has been approximately taken into account by scaling the model's solar constant input by the square of the Earth-Sun distance. The deviation of the lunar equatorial plane from the ecliptic (~5°) has a smaller effect and has been neglected in these computations.

The uncertainty of the computed disk temperatures was estimated by considering plausible variations in the Moon's principal thermophysical elements. For example, mean surface density variations lead to normal emissivities in the range 0.938–0.972 and correspond to disk-center brightness uncertainties of ±4 K. Accounting for errors in other regolith thermal and electrical properties, scattering due to subsurface inhomogeneities (Keihm 1982) and limb (high incidence angle) effects, Keihm arrived at an estimated overall accuracy of ±9 K in disk-averaged brightness temperatures from the model, corresponding to about 4% near ±90° phase at the DMR frequencies. Keihm estimated an additional diurnal uncertainty in the lunar flux of ~2% with phase.

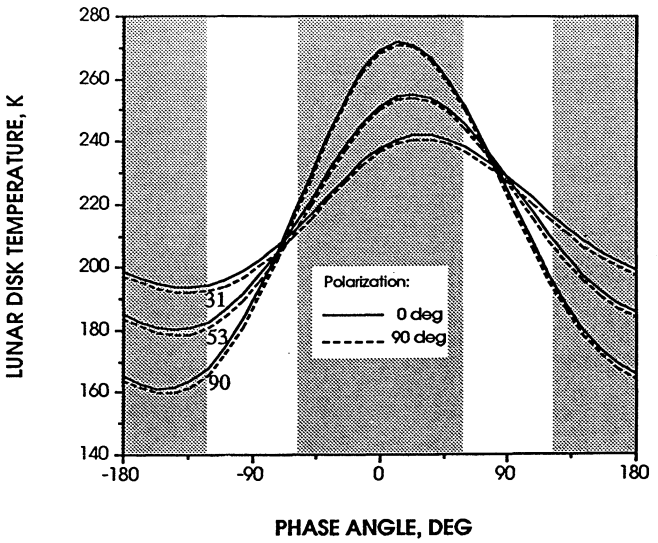

FIG. 5.—Model predictions of the lunar disk brightness temperature vs. phase at the DMR frequencies. The DMR does not sample the lunar disk temperature in the shaded regions.

We have adopted Keihm's model as an estimate of the lunar brightness temperature to allow a derivation of calibration, pointing, and beam pattern reconstruction, as described below.

3.3. *Analysis*

When the Moon is within 30° of the *COBE* orbital plane, it is observed many times by each DMR horn. Figure 6 shows the orbit tracks and center points of 0.5 s integrations in the vicinity of the Moon for a typical *COBE* orbit. The circles show the −3 dB and −10 dB signal level contours. The cross-hatching of the orbit tracks is caused by the passage across the Moon of the circular track swept by a DMR antenna axis as the spacecraft rotates. In general the path of the Moon intersects this circle twice per orbit.

We assume initially that variations in both spacecraft attitude errors and the calibrations of the DMR receivers are stable over sufficiently long periods of time to obtain statistically significant determinations of their values. The pointing error model allows for four errors: systematic offsets Δ_x and Δ_y in the direction of the spacecraft rotational axis from that given by the spacecraft aspect solution, and offsets from the nominal radial (θ) and rotational (ϕ) directions of each antenna beam relative to the spacecraft body obtained from prelaunch alignment measurements. The assumption that these quantities and the gain factors are quasi-stable allows their determination by a linear regression in which the measured data are compared with computed values based on spec-

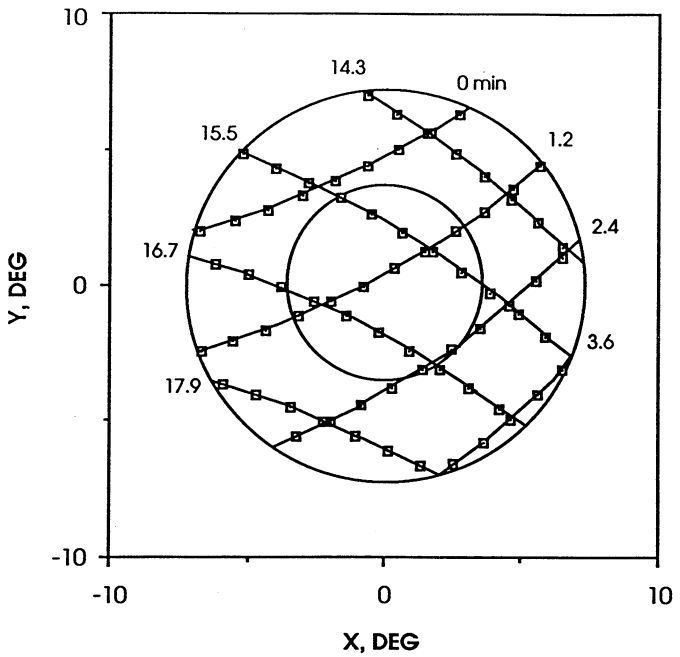

FIG. 6.—Distribution of lunar observations in the antenna beam during one orbit. The circles indicate 0.5 and 0.1 lunar signal level contours. The relative time, in minutes, is given for the beginning of each scan path.

ifications of the antenna patterns and the lunar brightness temperature model. In particular, we may write for the model antenna temperature for the ith observation made by one DMR antenna:

$$T_i = P(\theta_i) T_{\mathrm{Di}} \left(\frac{\Omega_m}{\Omega_b} \right), \tag{7}$$

where T_{Di} is the lunar disk temperature computed for the polarization of the ith observation, $P(\theta_i)$ is the normalized $[P(0) = 1]$ antenna gain pattern at an angular distance θ_i of the lunar brightness centroid from the beam center, Ω_m is the solid angle of the lunar disk, and Ω_b is the beam solid angle as given by

$$\Omega_b = 2\pi \sum_0^{\pi} P(\theta_i) \sin \theta_i \, d\theta_i , \tag{8}$$

where the sum over binned beam pattern data replaces an integral. Equation (7) is corrected for the fact that the Moon is observed against the 2.7 K cosmic background. The lunar analysis assumes that the antenna gain pattern is azimuthally symmetric. The angular distance, $\theta = \theta(\alpha_i, \delta_i, x, y, \psi, \Delta_x, \Delta_y, \Delta_\theta, \Delta_\phi)$, is a function of the pointing offsets defined above, where x and y are the nominal angular directions, ψ is the rotation angle of the spacecraft spin axis from the spacecraft ephemeris, and α_i and δ_i are the right ascension and declination of the Moon's centroid of emission. We form the least-squares sum

$$\sum_i (\mathfrak{G} S_i - T_i)^2 ,$$

where S_i is the ith uncalibrated lunar measurement made by the antenna in question, and $\mathfrak{G}$ is the calibration factor of the given channel and antenna. Each measurement S_i is approximately corrected to remove the small real difference signal from galactic emission and the cosmic dipole distribution using a preliminary map of the sky at the frequency in question and knowledge of the pointing vectors of the two antennas of a pair. An adjustment is also made using the antenna gain pattern to correct its value to the midpoint of the integration, allowing for the fact that the antenna beam scans an arc of 2°.4 during the 0.5 s integration. Minimization of this sum for variations of the parameters Δ_x, Δ_y, Δ_ϕ, Δ_θ, and $\mathfrak{G}$, for a given set of lunar observations, then yields optimum values for these parameters under the assumption that they are constant. Each sum is over ~ 600 data points corresponding to a time interval of about a day.

The analyzed data were restricted to observations with midpoints within 7° of the lunar brightness centroid, corresponding to lunar signals $\gtrsim 100$ mK. Spacecraft attitude corrections Δ_x and Δ_y for different channels are small and demonstrate that these are well separated from the determinations of individual horn alignment offsets Δ_ϕ and Δ_θ. The stability with time of the spacecraft attitude justifies the use of periods on the order of a day to determine the parameters.

The beam solid angle Ω_b that appears in equation 7 is a critical parameter in determining the gain factor, $\mathfrak{G}$, of each radiometer. Using the preflight patterns in an initial pass through the lunar observations, we derived pointing corrections and a collection of luner-derived measurements of the in-flight beam patterns out to an angle of 20° from the boresight. Figure 7 shows some representative plots of these data and the ground-based measurements of the beam patterns (Toral et al. 1989). The patterns obtained from both the lunar observations and ground range measurements were then numerically integrated to obtain the solid angles for each antenna given in Table 6. The 31A and 31B radiometers share the same pair of horns.

The lunar-derived pointing angles, the optical alignment measurements carried out during the final assembly of the spacecraft, and their total angular difference are listed in Table 7. The pointing angles of the common 31A and 31B horns are reproduced to less than 0°.05. Figure 8 provides the definition of the *COBE* spacecraft coordinate system.

Figure 9 shows the lunar-derived and noise source-derived calibration for the first year of flight. A clear monthly 5% phase-dependent systematic error exists in the lunar model, as seen in Figure 9. A smaller, 2% long term ($\approx$annual) error in the lunar calibration is also apparent. In general the noise source derived calibration is smoother; it appears more reliable than the lunar-derived calibration. Table 8 presents the results of the lunar calibration analysis by averaging the lunar-derived calibration systematic effects.

3.4. *Results and Discussion*

Lunar observations were used to determine the pointing for each of the DMR antennas, the antenna gain patterns, and the gain factors of the radiometer along with their variation with time.

The antenna gain patterns are seen to reproduce the ground range patterns within the accuracy of the flight measurement (Fig. 7). The flight-derived beam pattern solid angles reproduce the ground-measured solid angles with systematic deviations of less than 0.75% and rms deviations less than 1.5%. The flight pattern measurements become uncertain beyond $\sim 15°$ from the boresight, but 99.3% of the beam solid angle is within 15° of the beam center, as computed from the ground patterns. Given the fewer assumptions, simpler analysis, and higher

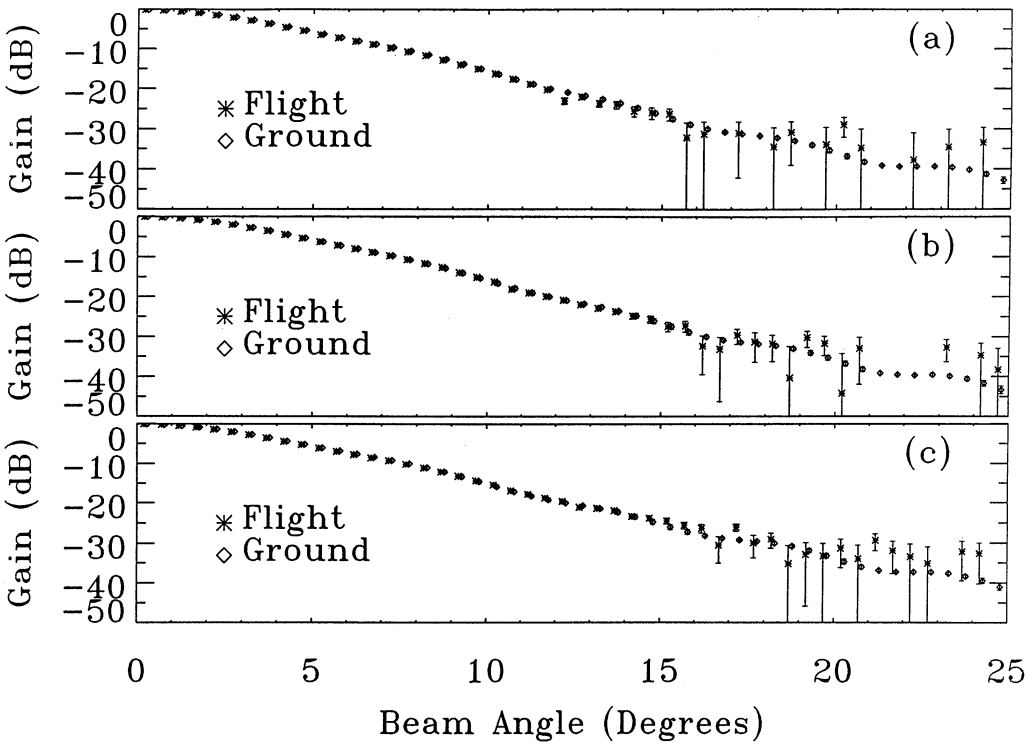

FIG. 7.—Comparison of antenna patterns from lunar observations and preflight antenna range measurements. Sample plots include (*a*) 31 GHz A channel horn number 1, (*b*) 53 GHz A channel horn number 1, and (*c*) 90 GHz A channel horn number 1.

signal-to-noise ratio of the ground measurements, we adopt the ground measurements for both the beam patterns and solid angle values for this paper. Analysis of the flight pattern measurements will continue.

The pointing correction solutions (Table 7) appear to be stable and are $\lesssim 3\%$ of the 7° FWHM beam for five of six pairs of horns, and $\lesssim 10\%$ for the 53B horn pair. Although all 6 DMR channels were designed to take data simultaneously, the 53B pointing error for both horns 1 and 2 imply a one minor frame (0.25 s) timing error. This conclusion is confirmed by a careful examination of the turn-on times of the noise sources between channels 53A and 53B. Table 7 gives values for the 53B ground pointing measurements with and without the 0.25 s timing correction.

TABLE 6

BEAM SOLID ANGLE MEASUREMENTS

Channel	Horn	Ω_b – Ground (deg^2)	Ω_b – Flight (deg^2)	% Difference Flight – Ground / Ground
31A, B	1	69.74 ± 0.35	67.7 ± 1.4	−2.9 ± 2.1
31A, B	2	69.74	69.7	−0.6
53A	1	68.21	66.7	−2.2
53A	2	68.99	68.3	−1.0
53B	1	69.04	68.4	−0.9
53B	2	68.88	69.0	1.7
90A	1	73.40	73.0	−0.5
90A	2	73.01	72.7	−0.4
90B	1	68.32	69.2	1.5
90B	2	68.04	68.8	1.1

The *mean* gain constant solutions, $\mathfrak{G}$ (Moon), are all within 4% of the noise-source–derived values (Table 8). The lunar-derived values are the average taken over systematic effects in the lunar model. The overall absolute uncertainty of the lunar model is not well determined. The lunar measurements provide assurance and comfort that the integrity of the system was

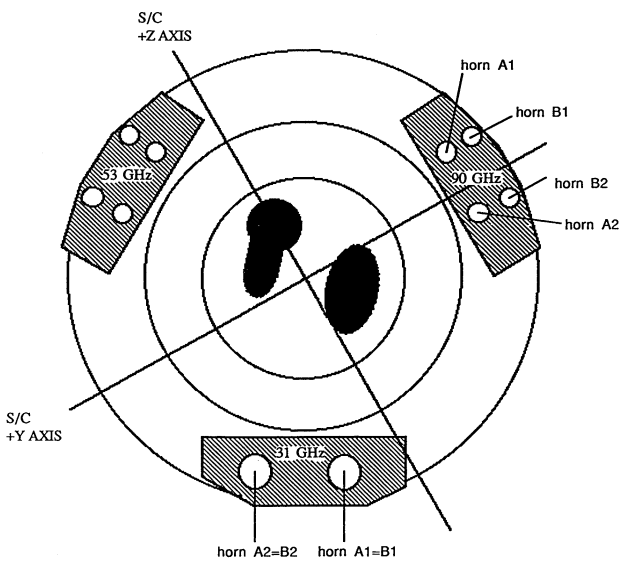

FIG. 8.—*COBE* spacecraft view (looking down from the sky) with coordinate system definition. The 53 GHz horn labels parallel those of the 90 GHz horns. The black "keyhole" is the FIRAS aperture and the black ellipsoid is the DIRBE aperture.

TABLE 7

COMPARISON OF GROUND-BASED AND FLIGHT-BASED DETERMINATIONS OF DMR HORN POINTING ANGLES[a]

Radiometer Channel and Horn	x Component	y Component	z Component	|Flight − Ground| Direction Difference (degrees)
31A Horn #1	−0.866300	−0.439242	−0.237889	0.20
	−0.866193	−0.437741	−0.241022	
31A Horn #2	−0.865935	0.426699	0.260929	0.19
	−0.866794	0.426828	0.257847	
31B Horn #1	−0.866300	−0.439242	−0.237889	0.20
	−0.865735	−0.438518	−0.241258	
31B Horn #2	−0.865935	0.426699	0.260929	0.20
	−0.866699	0.427148	0.257638	
53A Horn #1	−0.867114	0.430902	−0.249875	0.15
	−0.868316	0.429617	−0.247903	
53A Horn #2	−0.867207	−0.430773	0.249773	0.11
	−0.866251	−0.432353	0.250359	
53B Horn #1	−0.867549	0.430783	−0.248566	0.71
	−0.868104	0.435939	−0.237385	
	−0.867549	0.435894	−0.239490	0.13
53B Horn #2	−0.868383	−0.428613	0.249402	0.63
	−0.866978	−0.436007	0.241343	
	−0.868383	−0.433742	0.240371	0.17
90A Horn #1	−0.865087	−0.005668	0.501589	0.11
	−0.865959	−0.006199	0.500076	
90A Horn #2	−0.867054	−0.007587	−0.498156	0.07
	−0.866637	−0.006660	−0.498895	
90B Horn #1	−0.865705	−0.006400	0.500514	0.03
	−0.865835	−0.006344	0.500289	
90B Horn #2	−0.865779	−0.007480	−0.500371	0.12
	−0.865995	−0.009355	−0.499965	

NOTE.—The first row of direction cosines corresponds to the ground measurement and the second row corresponds to the flight measurement. The third row of numbers for the 53B channels correspond to the ground-based determination of the horn pointing angles corrected by a 0.25 s timing offset (see text).

[a] Direction cosines in spacecraft x, y, z coordinates.

maintained through launch and that there were no major changes in the calibration of the radiometers in the period between detailed calibration in the summer of 1988 through the Delta rocket launch of 1989 November. The lunar measurements also serve as an independent cross-check on the degree to which the "up" and "down" noise source amplitudes at each frequency could be varying with time.

4. IN-FLIGHT CALIBRATION FROM SEASONAL EARTH VELOCITY MODULATION OF THE DIPOLE

4.1. *Introduction*

Motion of the DMR instrument through the CMB radiation field produces a dipole anisotropy in the observed CMB intensity through the Doppler effect. *COBE* orbits the Earth at 7.4

TABLE 8

COMPARISON OF MEAN LUNAR-DERIVED AND NOISE SOURCE–DERIVED GAIN FACTORS

		$\Delta G/G$ (RELATIVE)		$\Delta G/G$ (ABSOLUTE)	
CHANNEL	G(MOON)/G(NOISE SOURCE)	Noise Source	Moon	Noise Source	Moon
31A	1.035	0.003	0.019	0.025	0.05
31B	0.981	0.004	0.018	0.023	0.05
53A	1.029	0.001	0.023	0.007	0.05
53B	1.029	0.002	0.023	0.007	0.05
90A	1.023	0.004	0.025	0.020	0.05
90B	1.039	0.003	0.026	0.013	0.05

NOTE.—G(Moon)/G(Noise Source) is the *mean* lunar calibration relative to the noise source calibration. The error is dominated by lunar phase-dependent and long-term (≈annual) systematic errors in the lunar model. Absolute brightness temperature lunar model systematic errors are estimated to be about 5%.

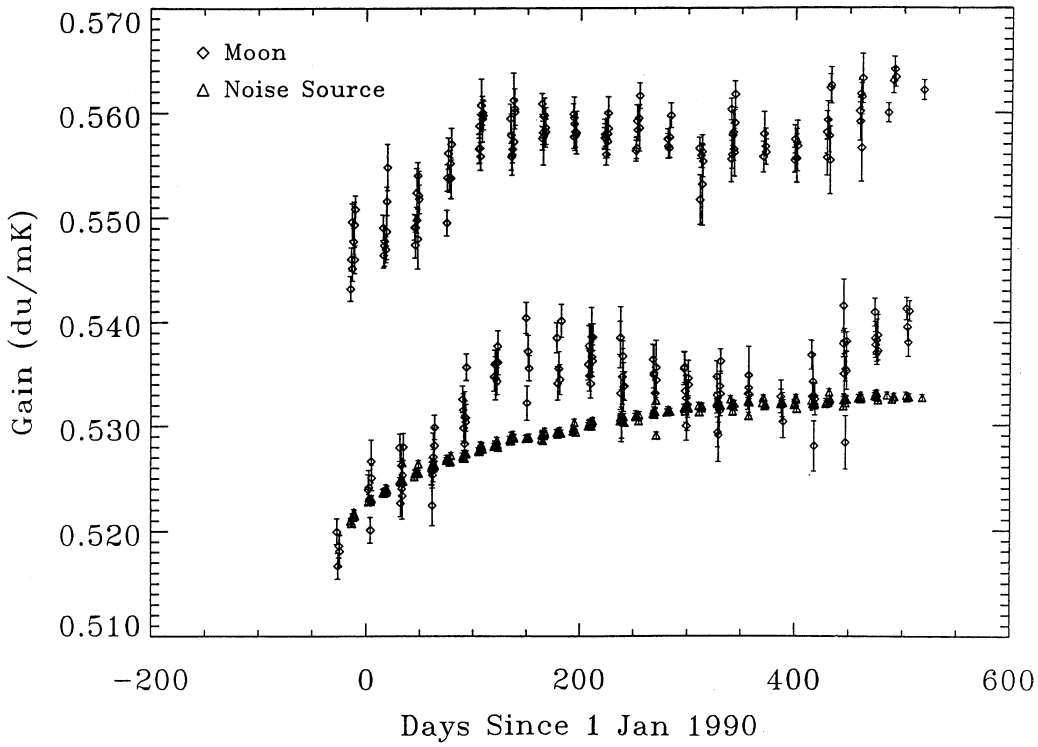

FIG. 9*a*

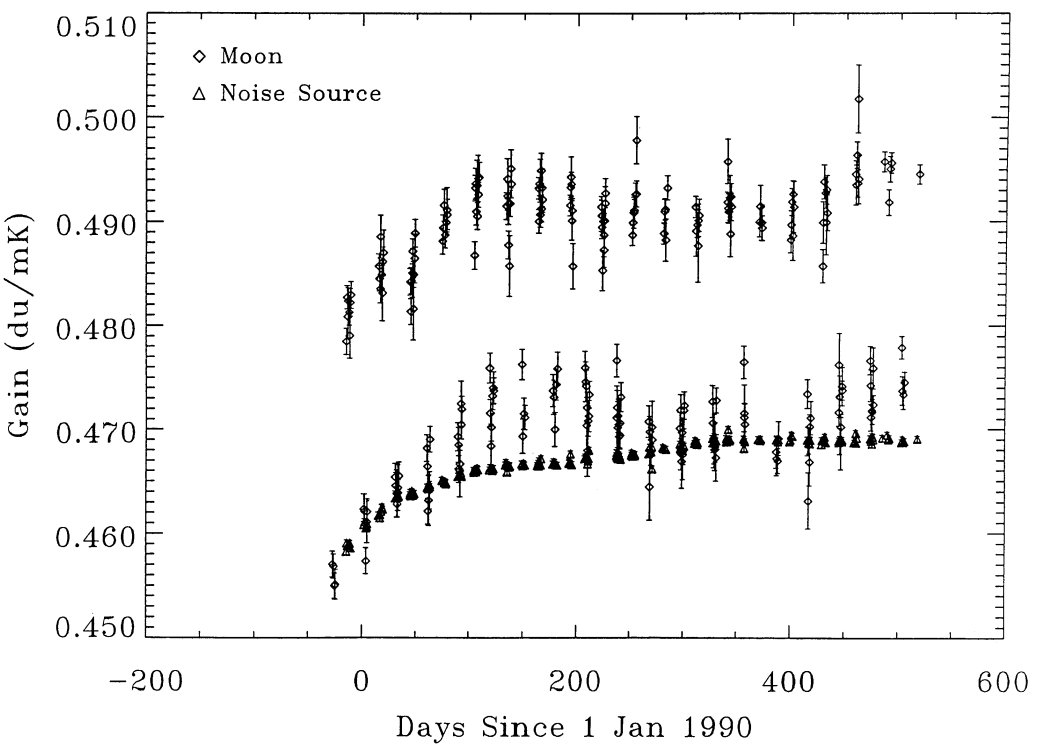

FIG. 9*b*

FIG. 9.—Lunar-derived and noise source–derived calibration as a function of time for the (*a*) 53 GHz A channel, and (*b*) 53 GHz B channel. What appears as two sets of Moon points is the two-week interleaved 5% lunar phase-dependent systematic error. A longer term (≈annual) 2% error is also seen.

km s^{-1}, 14 orbits per day, and the Earth orbits the barycenter of the solar system at 29.7 km s^{-1} once per (sidereal) year. Since these motions are accurately determined by independent means, their effect can be separated from the fixed astrophysical signals and used to calibrate the radiometer output. The periodic variation in $\Delta T/T$ of the dipole signal from these motions, though a small fraction of the total dipole anisotropy (Smoot et al. 1991), provides a direct calibration of the radiometers using the Doppler conversion. The *COBE* orbit around the Earth produces a modulation of 0.07 mK amplitude and the Earth orbital velocity produces a modulation of 0.3 mK amplitude, while the rms sensitivity for a year of observation is roughly 0.010 mK.

The *COBE* FIRAS experiment has demonstrated that the CMB radiation has a Planckian spectrum to a high degree of accuracy (Mather et al. 1990) so the complete form for the relativistic Doppler effect for a blackbody can be used (Peebles & Wilkinson 1968)

$$\frac{T(\theta)}{T_0} = \frac{(1-\beta^2)^{1/2}}{1-\beta\cos\theta} = 1 + \beta\cos\theta + \frac{\beta^2}{2}\cos 2\theta + O(\beta^3)\,. \quad (9)$$

From $\beta = 0.00122 \pm 0.00006$ (Smoot et al. 1991) the amplitude of the quadrupole term (third term) is 7.4×10^{-7} and can safely be neglected in the following discussion.

Figure 10 presents the observed dipole amplitude as a function of time due to the Earth's orbit about the barycenter of the solar system. (As discussed below, a correction has been made in each point for the effect of the satellite motion about the Earth.) The amplitude of the observed sinusoidal modulation can be compared with the value predicted by equation (9) to derive the absolute calibration of the instrument. Although this signal is measured daily at low signal-to-noise ratio, it has the advantages of being known a priori and of completely filling the antenna aperture. The plot also shows the fitted shape of the variation as a function of time.

4.2. *Technique*

The telemetry data from the spacecraft are read and checked for quality. Less than 1% of the data fail this test. A baseline is removed from the differential temperature signal and corrections are applied for the known systematic effects of the instrument (Smoot et al. 1991).

Before any long-term analysis is done on the data a check is made to ensure that the calibration of the instrument is not a function of time. The analysis of the noise source performance in flight, discussed earlier in § 2.3 limits any uncorrected drifts in the gain to $\delta\mathfrak{G}/\mathfrak{G} < 0.4\%$ in a year, assuming the two noise sources at a frequency do not drift in tandem with time. (We correct for the 90 GHz noise source change of 0.7%, discussed earlier.) We omit all data within 10° of the galactic plane and perform a least squares fit on the time-ordered data for (1) the amplitude of the dipole, with a time-variable direction, resulting from the combined *COBE* motion about the Earth and the Earth orbital motion about the solar system barycenter, (2) the amplitude and (time-fixed) direction of the dipole resulting from the motion of the barycenter of the solar system, and (3) the amplitude and (time-fixed) direction of any quadrupole terms. No significant quadrupole term exists (Smoot et al. 1991). We use the fitted amplitude of (1), above, to dervive the instrument calibration.

4.3. *Results*

The results of the analysis of the sinusoidal variation in the amplitude of the Earth-velocity modulation of the dipole is given in Table 9. We find that all of the Earth-velocity derived gain factors are consistent, within the statistical errors, with the ground-based noise source calibration solutions. The largest deviation occurs for the 53 GHz B channel radiometer, where the solutions are discrepant by ~5.3%, still less than a 2 σ deviation.

5. SUMMARY AND CONCLUSIONS

We have presented three independent methods for determining the calibration of the *COBE* Differential Microwave Radiometers. The definitive analysis of the noise source calibration has been presented in this paper. Two in-flight calibration techniques have been presented: (1) based on the microwave

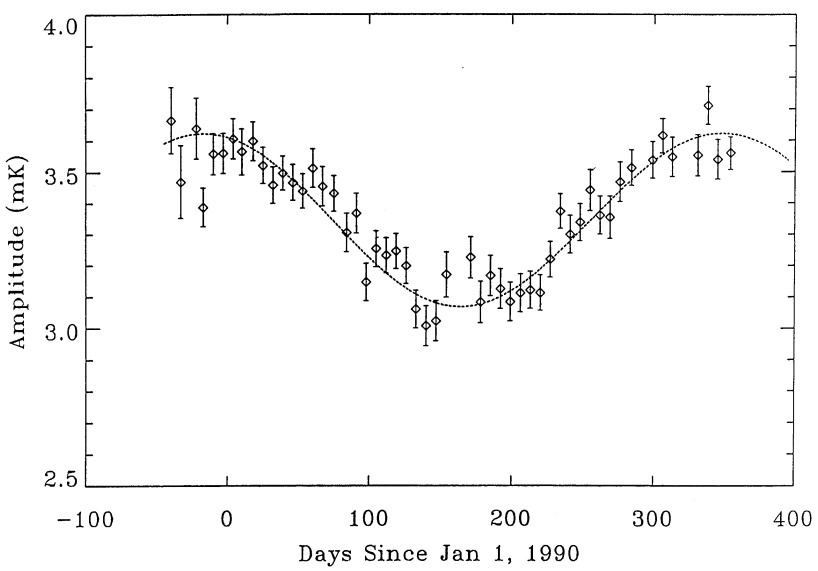

FIG. 10.—Earth velocity modulation of the dipole amplitude (Channel 53B) as a function of time. These plots show the fitted shape of the variation as a function of day number due to the Earth's revolution about the barycenter of the solar system. The amplitude provides an absolute calibration of the DMR.

TABLE 9

RATIOS OF EARTH-VELOCITY TO NOISE SOURCE DERIVED GAIN FACTORS

CHANNEL	$\mathcal{G}$(EARTH VELOCITY)/$\mathcal{G}$(NOISE SOURCE)	$\Delta\mathcal{G}/\mathcal{G}$ (ABSOLUTE)	
		Noise Source	Earth Velocity
31A	0.992	0.025	0.068
31B	1.005	0.023	0.066
53A	1.000	0.007	0.028
53B	0.946	0.007	0.032
90A	1.048	0.020	0.054
90B	1.030	0.013	0.041

signal from the Moon, and (2) based on the microwave signal caused by the Earth-velocity Doppler-shifted CMB. The analyses of these two in-flight techniques are not final since the DMR continues to collect data, and current results will be improved.

The amplitude of the 3.3 mK dipole signal determined by the two independent DMR receivers at each of the three frequencies provide a consistency check on each of the calibration solutions. Table 10 summarizes this check. It is important to note that in the case of the Moon taking such a ratio cancels the effect of any error in the overall microwave brightness temperature of the Moon as well as other potential lunar analysis systematic errors. In the case of the 31 GHz radiometer, the A and B channels observe different polarizations so some real nonunity ratio cannot be ruled out.

Table 11 presents a comparison of the present accuracy of the three calibration techniques. The noise source technique results in 1%–3% absolute (depending on channel) and less than 0.4% per year relative calibration errors. The absolute lunar calibration appears to be accurate to $\sim$5%, while systematic errors can be averaged with time to provide about 2% relative calibration uncertainty. The Earth velocity Doppler technique currently provides a 3%–7% absolute calibration, but does not lend itself well to relative calibration.

It is important to emphasize that while an accurate *absolute* calibration is desirable for many purposes (such as for comparison with external measurements in attaining accurate galactic emission models, specifying the amplitude of anisotropies, etc.), it is the ability to correct in-flight variations in the calibration, i.e., *relative* calibration, that may limit anisotropy measurements. We have found that the in-flight calibration is stable and that small variations in the calibration can be measured and corrected.

TABLE 10

DIPOLE AMPLITUDE RATIOS BETWEEN CHANNELS AT THE SAME FREQUENCY BASED ON THREE TECHNIQUES

Ratio	Noise Source[a]	Moon[b]	Earth-Velocity[c]
31A/31B	1.06 $\pm$ 0.04	1.00 $\pm$ 0.03	1.07 $\pm$ 0.10
53A/53B	1.00 $\pm$ 0.01	1.00 $\pm$ 0.02	0.95 $\pm$ 0.04
90A/90B	0.99 $\pm$ 0.01	1.01 $\pm$ 0.04	0.97 $\pm$ 0.06

[a] Errors are the combined errors in the dipole solution and in the ground-based noise source calibration.

[b] Errors are the combined errors in the dipole solution and in the Moon calibration.

[c] Errors are combined errors in the dipole solution and in the Earth-velocity calibration.

TABLE 11

$\Delta\mathcal{G}/\mathcal{G}$ FOR THE THREE TECHNIQUES

CHANNEL	NOISE SOURCE		MOON[a]		EARTH-VELOCITY
	Relative (%)	Absolute (%)	Relative (%)	Absolute (%)	Absolute (%)
31A	0.3	2.5	1.9	5.	6.8
31B	0.4	2.3	1.8	5.	6.6
53A	0.1	0.7	2.3	5.	2.8
53B	0.2	0.7	2.3	5.	3.2
90A	0.4	2.0	2.5	5.	5.2
90B	0.3	1.3	2.6	5.	4.1

[a] The relative lunar calibration error is dominated by the 5% phase-dependent and 2% long-term ($\approx$annual) systematic effects.

We summarize our findings.

1. We have presented the final analysis of the DMR laboratory calibration of the noise sources. (*a*) To within $\sim$2% errors, the ground calibration appears to remain valid in flight, and constitutes the best calibration at this time. (*b*) The noise source variations in flight are less than 0.4% per year, assuming that the noise source amplitudes are not varying in tandem with time [see 2(*f*) below].

2. We have presented a preliminary analysis of the use of the Moon as an in-flight calibrator. (*a*) The Moon model has a 5% peak-to-peak lunar phase-dependent systematic error. (*b*) The Moon has a 2% peak-to-peak long term ($\approx$annual) systematic error. (*c*) We estimate the overall accuracy of the absolute lunar calibration at 5%. (*d*) The beam gain patterns (and solid angles) measured using the Moon confirm that the ground range measurements are valid in flight. The range measurements have higher signal-to-noise ratio and smaller potential systematic errors, and thus are adopted both for the patterns and the beam solid angles at this time. Further analysis of the in-flight measurements will continue. (*e*) The pointing corrections from the lunar analysis agree with the ground measurements to $\lesssim$0°.2 ($\lesssim$0.03 of the 7° FWHM beamwidth), after correcting the 53B channel for a 0.25 s timing offset. (*f*) The lunar calibration sets an upper limit of a couple of percent on the common-mode variation of the two independent noise sources at each frequency (see Table 11).

3. We have presented a preliminary analysis of the use of the Earth-velocity Doppler effect signal as a calibrator. (*a*) The Earth-velocity calibration provides the best check on the noise source-derived absolute calibration of the radiometers. With sufficient future observing time the Earth-velocity derived absolute calibration accuracy may approach that of the noise source calibration. (*b*) The Earth-velocity calibration sets an upper limit of a few percent on the common-mode variation of the two independent noise sources at each frequency (see Table 11).

4. We have compared the three calibration techniques and presented the overall calibration uncertainty results in Table 11. At present we regard the noise source gain factor calibration (Tables 4 and 11) as the best DMR calibration; however, the uncertainties in the other techniques will decrease with time.

We are grateful to the NASA *COBE* Project for their support of this work. We wish to thank the many people at the NASA/Goddard Space Flight Center who assisted with this work. In particular, we thank: C. Albert, J. Aymon, M. Bukowski, S. Chintala, J. Chitwood, T. Erickson, D. Fadler,

L. Hilliard, S. Kaltenbaugh, B. Klein, V. Kumar, J. Lecha, M. Lecha, S. Leete, P. M. Lubin, J. Marushak, S. Masiee, R. Mattson, D. McCarthy, P. McCaslin, D. McDermont, S. S. Meyer, R. Mills, D. Nace, P. Pashbe, R. Patschke, F. Patt, D. Pham, A. Rae, R. Ratcliff, C. Richards, H. Sampler, R. Weber, D. West, J. Wolfgang, E. Young, and P. Young.

REFERENCES

Evans, G., & McLeish, C. W. 1977, RF Radiometer Handbook (Dedham, MA: Artech House)
Gulkis, S., Lubin, P. M., Meyer, S. S., & Silverberg, R. F. 1990, Sci. Am., 262, No. 1, 132
Keihm, S. J. 1982, Icarus, 53, 570
———. 1983, JPL Internal Memo, May 2, 1983
Keihm, S. J., & Gary, B. L. 1979, Proc. 10th Lun. Planet Sci. Conf., 2311
Keihm, S. L., & Langseth, M. G. 1975, Icarus, 24, 211
Kraus, J. D. 1966, Radio Astronomy (New York: McGraw-Hill)
Mather, J. C. 1982, Opt. Engineering, 21, 769
Mather, J. C., et al. 1990, ApJ, 354, L37
Mather, J., & Kelsall, T. 1980, Phys. Scripta, 21, 671
Peebles, P. J. E., & Wilkinson, D. T. 1968, Phys. Rev., 174, 2168
Smoot, G. F., et al. 1990, ApJ, 360, 685
Smoot, G. F., et al. 1991, ApJ, 371, L1
Toral, M. A., Ratcliff, R. B., Lecha, M. C., Maruschak, J. G., Bennett, C. L., & Smoot, G. F. 1989, IEEE Trans. Ant. Prop., 37, 171